

Finite Element analysis of post-tensioned SG-laminated glass beams with adhesively bonded steel tendons

Bedon, Chiara; Louter, Christian

DOI

[10.1016/j.compstruct.2017.01.086](https://doi.org/10.1016/j.compstruct.2017.01.086)

Publication date

2017

Document Version

Final published version

Published in

Composite Structures

Citation (APA)

Bedon, C., & Louter, C. (2017). Finite Element analysis of post-tensioned SG-laminated glass beams with adhesively bonded steel tendons. *Composite Structures*, 167, 238-250.
<https://doi.org/10.1016/j.compstruct.2017.01.086>

Important note

To cite this publication, please use the final published version (if applicable).
Please check the document version above.

Copyright

Other than for strictly personal use, it is not permitted to download, forward or distribute the text or part of it, without the consent of the author(s) and/or copyright holder(s), unless the work is under an open content license such as Creative Commons.

Takedown policy

Please contact us and provide details if you believe this document breaches copyrights.
We will remove access to the work immediately and investigate your claim.



Finite Element analysis of post-tensioned SG-laminated glass beams with adhesively bonded steel tendons



Chiara Bedon ^{a,*}, Christian Louter ^b

^a University of Trieste, Department of Engineering and Architecture, Piazzale Europa 1, 34127 Trieste, Italy

^b Department of Architectural Engineering and Technology, Faculty of Architecture and the Built Environment, Delft University of Technology (TU Delft), Delft, The Netherlands

ARTICLE INFO

Article history:

Received 27 September 2016

Revised 19 November 2016

Accepted 11 January 2017

Available online 7 February 2017

Keywords:

Finite Element numerical modelling

Experimental testing

Laminated glass

Adhesive joint

Steel tendon

Post-tensioning

Bending performance

ABSTRACT

Taking advantage of past full-scale experimental test results, the bending performance of laminated glass beams with post-tensioned, adhesively bonded steel tendons is explored via refined Finite-Element (FE) models. As far as the primary advantage of the post-tensioned glass beam concept is to provide an initial state of compressive stresses in glass, a marked enhancement of the expected structural performance is expected (i.e. increase of the initial fracture load and redundancy), compared to typically brittle, unreinforced laminated glass beams. Several key aspects can affect the overall performance of such beam typology, first of all the adhesive joint providing the structural interaction between the glass beam and the steel tendon, as well as the geometrical and mechanical properties of each beam component, in relation to the amount of initial post-tensioning force. Based on a first validation of a reference full 3D FE model towards the available past full-scale experimental test results, an extended parametric study is presented in this paper, giving evidence to the effects of several mechanical and geometrical parameters (i.e. steel tendon section, level of the applied post-tensioning force, adhesive joint type and size, etc.) in the bending performance of post-tensioned laminated glass beams at room temperature under quasi-static load.

© 2017 Elsevier Ltd. All rights reserved.

1. Introduction

In this paper, an extended Finite Element (FE) analysis is proposed to assess the structural in-plane bending performance of post-tensioned laminated glass beams with adhesively bonded steel tendons. In accordance with some reference experimental test results available in literature [1], these post-tensioned glass beams typically consist of a laminated glass web, a bottom stainless steel post-tensioning tendon and an adhesive layer interposed between the tensile (bottom) edge of the laminated glass beam and the steel tendon itself.

Due to the typical tensile brittle nature of glass as well as to its increasing use in buildings and facades in the form of load-bearing structural components – aiming to fully exploit the potential of this rather innovative construction material – the concept of post-tensioned glass beams with steel cables or tendons has been already investigated in the past years. A rather limited number of experimental research projects [2–6] and applications in practice [7] are available, however. The feasibility and potential of laminated glass beams with post-tensioning, adhesively bonded carbon

fiber polymer (CFRP) tendons has been also experimentally assessed [5,6]. Some Finite Element extended investigations are also available for the explored post-tensioning design concept [8,9].

Since glass is relatively weak in tension but strong in compression [10], the primary advantage of adding post-tensioning tendons to laminated glass assemblies is to apply a beneficial compressive pre-stress, hence – for the beams object of investigation in the current paper – to enhance the expected overall performance by increasing the initial fracture strength. Secondly, the post-tensioning tendons typically provide safe post-fracture performance and redundancy, since upon fracture of glass the tendons are expected to bridge the cracks and transfer the tensile forces over the cracks themselves. This generates, given a reference post-tensioned glass beam in bending, an efficient internal moment capacity between the tendon and the compressed (top) region of glass, thereby providing the beam significant post-fracture load-carrying performance and ductility.

The post-tensioning of steel or FRP tendons and cables either mechanically anchored or adhesively bonded to glass beams presents a further extension and optimization of the reinforced glass design concept, for which a comprehensive state-of-the-art overview is provided in [11,12].

* Corresponding author.

E-mail address: bedon@dicar.units.it (C. Bedon).

In this paper, based on the past experimental study presented in [1], a further attempt to rationally simulate, explore and optimize the structural response of post-tensioned laminated glass beams with adhesively bonded steel tendons is carried out through advanced, full 3D FE numerical models implemented in the ABAQUS computer software [13].

A short recapitulation of the reference experimental test results is first provided, together with the validation and assessment of the corresponding FE numerical model (M0, in the following sections). The so obtained FE predictions are compared to the test results and critically discussed. As shown, a key role is assigned to a multitude of aspects, including the appropriate description of all the assembling and testing phases (i.e. post-tensioning of the steel tendon followed by bonding with the laminated glass beam and subsequent release of the steel tendon, and successive in-plane bending simulation of the full post-tensioned composite assembly), as well as the accurate mechanical calibration of all the materials and the structural interaction between the specimens components.

Subsequently, the same FE modelling approach is further extended and a parametric FE study – aimed to assess and further optimize the global structural performance of the examined structural typology – is presented. The effects of mechanical as well as geometrical aspects are highlighted, including variations in the steel tendon section, modifications in the adhesive type and thickness, application of different levels of post-tensioning force.

As a first stage of an ongoing research study, based on the available full-scale experimental results, post-tensioned beams subjected to quasi-static monotonic bending loads and room temperatures are taken into account only.

2. Brief summary of past experimental tests

The current research investigation takes advantage of an exploratory experimental study recently carried out at École Polytechnique Fédérale de Lausanne (EPFL) on post-tensioned laminated glass beams with adhesively bonded steel tendons [1]. Within that study, which comprised of eight specimens in total, a series of three full-scale glass beams with adhesively bonded post-tensioning steel tendons were tested in four-point bending.

The typical post-tensioned beam investigated in this paper, having a total span $L = 1500$ mm, consists of a laminated glass (LG) beam composed of three polished edges layers of annealed float glass (6 and 10 mm the nominal thickness of external and middle layers respectively), with a nominal height of 125 mm. Bonding of the glass layers is achieved via SentryGlas® (SG) sheets with nominal thickness 1.52 mm. For the stainless steel tendon (grade 1.4301), a solid cross-section with 25 mm width and 3 mm the thickness is used. An adhesive layer, 0.1 mm in nominal thickness, composed of a two-component epoxy adhesive (3M Scotch-Weld DP490 [14]), is finally interposed between the LG beam and the bottom steel tendon, to provide an appropriate structural interaction between them. At a preliminary stage of the experimental program, the post-tensioned specimens were subjected to an initial post-tensioning force $P_0 = 30$ kN.

Fig. 1 presents the typical cross-section for such specimens, while an overview of the test setup, loading scheme and measured load-deflection curves is summarized in Fig. 2. Additional details related to the assembly and testing of the full-scale experimental specimens can be found in [1].

While the past literature contribution [1] presented a full-scale experimental validation of such design concept, including the comparison with fully unreinforced glass beam specimens (Fig. 1(a)) or post-tensioned beams with mechanically anchored tendons, this research paper focuses on the beam specimens with adhesively

bonded, post-tensioning steel tendons, as given in Fig. 1(b), including a critical comparison of experimental and Finite-Element numerical results, as well as an extended parametric investigation.

Based on [1], in particular, given a cross-section like Fig. 1(b) and the test setup of Fig. 2(a), the effect of an assigned initial post-tensioning force P_0 for the steel tendon is expected to manifest in the form of an upward deflection of the fully composite beam, with a corresponding bi-triangular distribution of initial stresses having maximum compressive (absolute) values at the bottom edge of the specimen. Assuming the in-plane bending loads are applied in accordance with the test setup of Fig. 2, in the hypothesis of a fully structural interaction between the LG beam and the steel tendon, the first tensile cracking of glass can be hence prevented as far as the total effect of post-tensioning and bending loads does not exceed the reference tensile resistance of glass σ_{tk} . Furthermore, the actual bending resistance is expected to depend on several mechanical and geometrical aspects, such as the type of glass (i.e. in the case any pre-stressing treatment is used rather than annealed float glass only), as well as the cross-section geometry, beam size and reinforcement percentage, as also studied in [15] for reinforced glass beams. For the current study, however, the main interest in this respect is to investigate the effects of the level of post-tensioning force in the steel tendon on the initial cracking resistance of the post-tensioned glass beams. The post-cracked stage takes in fact further advantage from the steel tendon alone.

The past experimental study presented in [1] typically emphasized the high potential of the explored design concept, with beneficial effects of the post-tensioning tendon – compared to the unreinforced LG section alone – but also in a significant post-fracture resistance and typically ductile collapse mechanism (see Fig. 2(b)).

3. Finite-Element numerical investigation

Based on the available experimental test results [1], an extended investigation of the same design concept was carried out in this paper by means of geometrically and mechanically refined, full 3D solid FE models implemented in the ABAQUS computer software [13], see Fig. 3.

3.1. FE model assembly of the reference model (M0) and solving approach

The FE exploratory investigation was performed by giving careful attention to several aspects, including the mechanical calibration of the constitutive laws for the materials (steel, glass, SG, adhesive), the FE description of the post-tensioning phase and related effects on the full composite assembly, as well as the implementation of an appropriate mechanical interaction between the steel tendon and the laminated glass beam (see also Section 3.3 for further details).

For this purpose, the typical FE model consisted of 3D solid elements for (i) the laminated glass beam, (ii) the stainless steel tendon and (iii) the adhesive layer.

In terms of geometrical features, the nominal dimensions were considered for all the specimens components, see Section 2. 8-Node, brick elements (C3D8R type) available in the ABAQUS library were then used. In doing so, two major meshing approaches were taken into account for each beam component, i.e. a free meshing technique for the laminated glass beam and a regular mesh pattern for the steel tendon and the adhesive layer. In the first case, the average size of the brick elements was set in the range comprised between 1.5 mm and 30 mm (with dense mesh pattern at the tensile edge of the beam, see Fig. 3), in order to

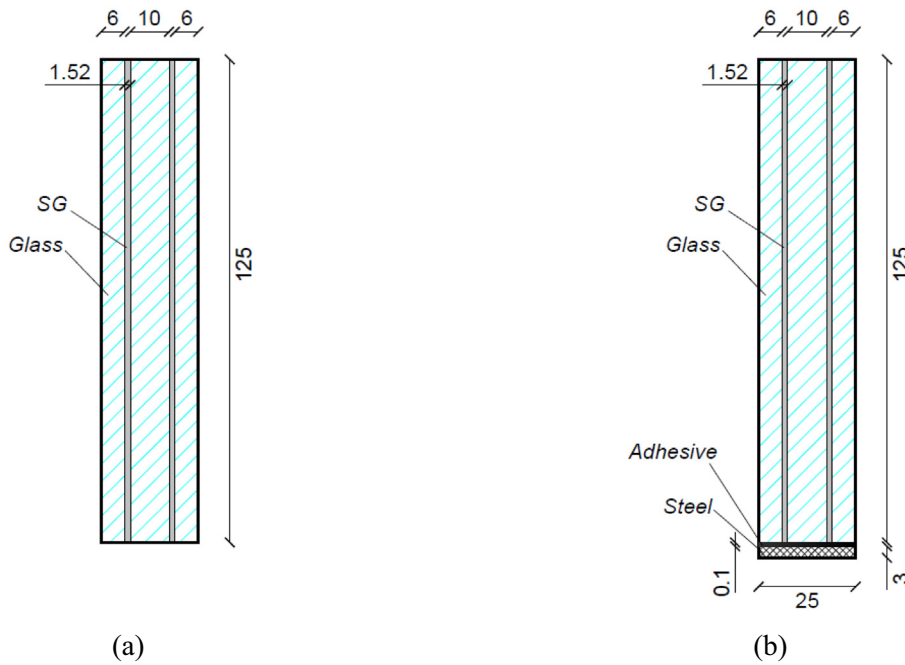


Fig. 1. Transversal cross-sectional properties for the experimental test specimens object of investigation, in accordance with [1]. (a) Reference, unreinforced glass beam and (b) post-tensioned beam. Nominal dimensions given in millimetres.

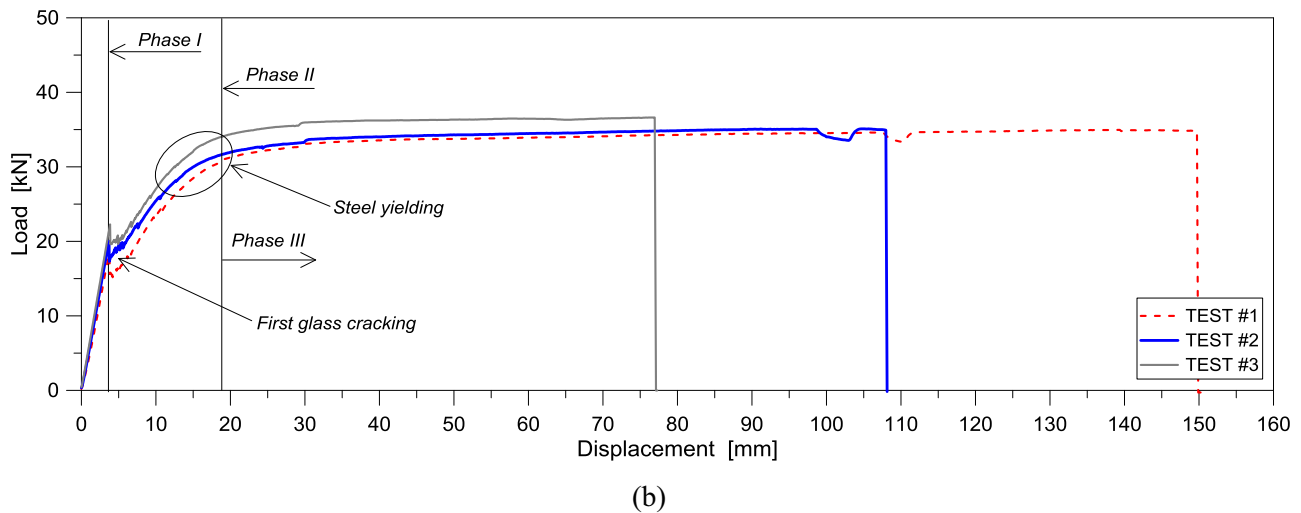
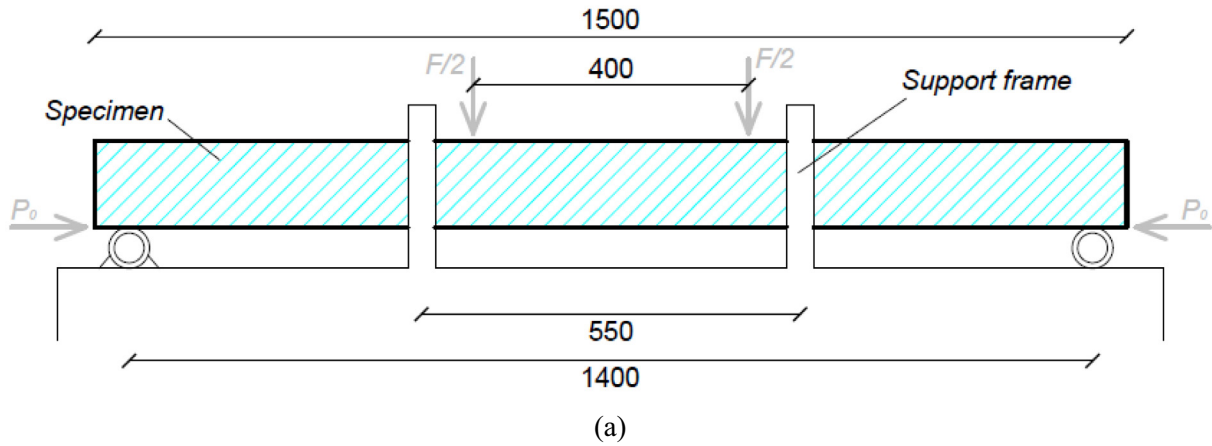


Fig. 2. Reference experimental bending tests on post-tensioned laminated glass beams with adhesively bonded steel tendons [1]. (a) Schematic overview of the loading protocol and test setup (front view), with (b) the corresponding measured load-deflection curves.

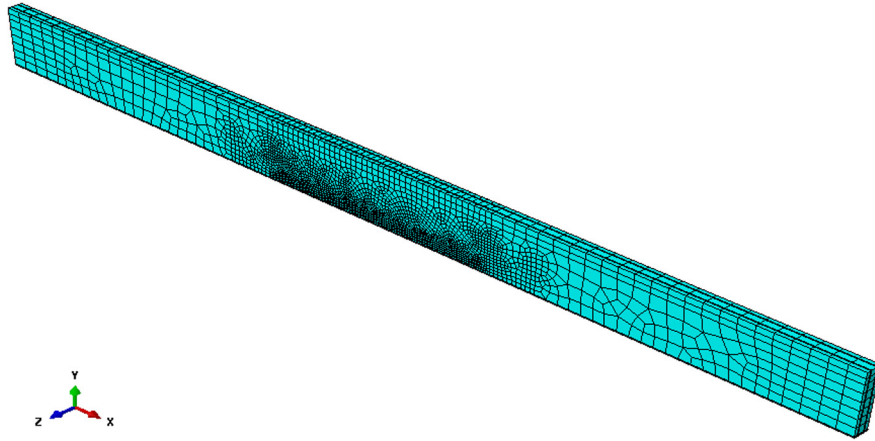


Fig. 3. Axonometry of the reference (M0) full 3D Finite-Element model of the reinforced, post-tensioned glass beams (ABAQUS [13]).

properly capture the tensile cracking phenomena in the glass layers when subjected to in-plane bending deformations, as well as to preserve the computational efficiency of the FE model.

For the stainless steel and adhesive layers, conversely, the average mesh size was set equal to 10 mm, including two solid elements in the thickness of each layer. As a result, the full FE assembly consisted of $\approx 140,000$ brick elements and $\approx 60,000$ DOFs (degrees of freedom).

3.2. Materials

The mechanical characterization of the constitutive laws for all the materials was based on several sources, including past literature references as well as results of available experimental tests carried out on small scale specimens and technical data sheets.

3.2.1. Annealed glass

For annealed glass, based on the provisions given by the available product standards [10], the nominal value for the characteristic tensile strength $\sigma_{tk} = 45$ MPa was taken into account. An homogeneous, linear elastic, isotropic material was defined, with nominal values [10] for the modulus of elasticity ($E_{glass} = 70$ GPa) and the Poisson ratio ($\nu_{glass} = 0.23$).

Careful consideration was then paid to the possible brittle failure in tension of the glass layers, being of primary importance for the post-cracks performance assessment of the examined beam typology, by means of the *brittle cracking* damage model with its *brittle shear* and *brittle failure* sub-options [13]. In the brittle cracking damage model, a Rankine failure criterion is used for the crack detection. As such, glass is consequently assumed to behave linear elastically until the maximum principal tensile stress exceeds the tensile strength σ_{tk} . Being a smeared model, the brittle cracking option does not track individual macro cracks, but the presence of cracks – having surface of propagation perpendicular to the direction of maximum principal stresses – is taken into account in the constitutive calculations performed at each material point, in the form of stress and stiffness degradation. The key input parameters of this damage model are hence represented the tensile strength of glass and its fracture energy.

In the current FE study, the input parameters for the damage model were derived from past literature contributions and recent applications to structural glass systems, see for example [9,16]. Given the nominal characteristic value ($\sigma_{tk} = 45$ MPa), for the fracture energy a reference value $G_f = 3$ J/m² was taken into account [17].

Regarding the post-cracked behavior of glass and the related *brittle shear* and *brittle failure* sub-options, through the FE analysis the cracked shear modulus of glass $G_{c,glass}$ was basically estimated as a fraction of the uncracked shear modulus G_{glass} :

$$G_{c,glass} = \beta(\varepsilon_{nn}^{ck}) \cdot G_{glass}, \quad (1)$$

with

$$0 \leq \beta(\varepsilon_{nn}^{ck}) = \left(1 - \frac{\varepsilon_{nn}^{ck}}{\varepsilon_{max}^{ck}}\right)^p \leq 1 \quad (2)$$

the shear retention factor, whose non-constant value depends on the crack opening strain ($\beta = 0$ denoting complete loss of aggregate interlock and $\beta = 1$ signifying the uncracked stage).

In Eqs. (1) and (2), ε_{nn}^{ck} and ε_{max}^{ck} represent the actual and ultimate crack opening strains respectively. The parameter p , based on earlier calibration [16], was finally assumed equal to $p = 5$.

A further advantage of the adopted damage material model is given – together with the evolution of damage specified by Eqs. (1) and (2) – by the implementation of a physical limit strain or displacement representative, for damaged elements, of the actual condition associated to their failure. In this paper, this effect was taken into account via the *brittle failure* sub-option, in which the ultimate displacement for cracked glass elements was set equal to [16]:

$$u_{ck} = \frac{2G_f}{\sigma_{tk}}. \quad (3)$$

In doing so, to avoid additional numerical instabilities in the post-cracked stage, the physical deletion of cracked elements from the mesh was fully disregarded. As such, failed glass elements with null residual stiffness and strength were not removed from the 3D assembly. In terms of post-processing of the obtained FE data, consequently, the first occurrence of tensile damage as well as the propagation of cracks in the LG beam up to collapse was monitored in the form of damage energy evolution and tensile stresses distribution in the glass elements.

3.2.2. SentryGlas[®], stainless steel and adhesive

Regarding the other FE model components, the implementation of constitutive laws for the materials was mainly derived from reference values available in literature from past experimental studies or FE investigations.

For the SG interlayer foils, despite their typical viscoelastic mechanical behavior, an equivalent constitutive law was used, as

also in agreement with [9,16,18,19]. Based on the experimental test results provided in [20], an elasto-plastic stress-strain relationship was used. The Poisson coefficient was set equal to $\nu_{SG} = 0.49$.

For the stainless steel tendon, an elasto-plastic stress-strain relationship was also taken into account. Based on [21], the elastic modulus was set equal to $E_{steel} = 200$ GPa, with $\nu_{steel} = 0.23$ the Poisson ratio, while the yielding/ultimate stress at failure was derived from small scale experimental test results $\sigma_y = \sigma_u = 860$ MPa [1]. The maximum strain at collapse, in accordance with [21], was finally assumed equal to 45%.

For the adhesive layer (3M Scotch-Weld DP490 type [14]), finally, a linear elastic constitutive law was implemented in ABAQUS, with $E_{adh} = 660$ MPa and $\nu_{adh} = 0.38$ the modulus of elasticity and Poisson ratio respectively, as experimentally obtained in [22]. This latter assumption for the mechanical behavior of adhesive was found to be reasonable, for the adhesive type of interest for the actual research study. In accordance with [22], the experimental response of 3M DP490 Epoxy specimens was found in fact to be almost linear up to failure.

3.3. FE implementation of post-tensioning phase, adhesive bonding stage and in-plane bending test

A key role was assigned to the mechanical interactions between the FE model components, so that the post-tensioning stage alone and its effects on the fully composite assembly could be properly described and taken into account for the simulation of the in-plane bending performance for the examined beams.

The typical simulation consisted, consequently, in a combination of three subsequent steps carried out both in ABAQUS/Standard and ABAQUS/Explicit [13], and namely represented by (I) pre-stressing of the steel tendon alone; (II) release of the tendon & adhesive bonding phase; (III) bending test. In the latter case, due to the dynamic nature of the adopted solver, careful consideration was paid in order to reproduce quasi-static loading conditions, as in the case of the reference experimental tests.

In terms of FE model assembly, through the full FE simulation process, a fully rigid connection was taken into account at the interface between the glass layers and the interposed SG foils, as well as at the interface between the so assembled LG beam (bottom face) and the adhesive layer (top face). Any possible delamination was thus fully disregarded at this current stage of the research activity. In the case of the adhesive-to-glass connection, however, the amount of maximum stresses was properly checked in the post-processing stage, in order to check the validity of these FE modelling assumptions (see Sections 4 and 5).

For each phase of the typical FE analysis, i.e. (I) to (III) phases, an appropriate combination of additional mechanical interactions, imposed loads/displacements and assigned nodal boundary conditions was also taken into account.

First, step (I), the post-tensioning phase was numerically reproduced in the form of a static incremental analysis. At this stage, the average experimental value of the imposed post-tensioning force P_0 was assigned to the steel tendon only, by means of an imposed equivalent longitudinal displacement (x -direction, in accordance with the reference system of Fig. 3). During this step, no mechanical interaction was considered between the steel tendon and the upper LG beam and adhesive layer, being the steel tendon able to axially deform and to slide freely along the bottom surface of the adhesive joint. In this regard, since the introduction in the steel tendon of the post-tensioning force P_0 was numerically described in the form of an imposed equivalent longitudinal deformation, the initial length of the steel tendon itself as well as the corre-

sponding mesh scheme was also properly defined and modified – compared to the nominal total span L of the M0 model – in order to provide an appropriate match with the upper adhesive layer mesh at the end of the post-tensioning procedure only (i.e. end of step (I)).

Once attained the desired level of initial prestress in the steel tendon alone, the release & adhesive bonding stage was reproduced in the form of a second static incremental step (phase (II)). In doing so, simple support restraints were assigned at the steel tendon ends, in accordance with the test setup proposed in Fig. 2. A *surface-to-surface* contact interaction was then imposed at the interface between the steel tendon (top surface) and the adhesive layer (bottom face). As in the case of the glass-to-SG and laminated glass-to-adhesive contact interactions previously described, a fully rigid connection was taken into account (i.e. null relative displacements and rotations among the interested mesh nodes of the steel and adhesive brick elements). The primary aim and consequence of this FE assumption is that the steel tendon, once released, could exhibit its effects in the form of an imposed upward bending for the above LG beam and a corresponding bi-triangular distribution of initial stresses in the glass layers, as also shown in Fig. 4.

In the specific case of the reference M0 model, the maximum uplift of the mid-span section due to post-tensioning only was found to be in the order of ≈ 1 mm (see Fig. 4(a)), with compressive and tensile stresses in the glass layers up to ≈ -28 MPa and $\approx +11$ MPa respectively (see Fig. 4(b)). Compared to [1], where a simple analytical model was also presented, a close correlation was found with the numerically predicted initial state of stresses in glass, i.e. being the theoretical expected stress values in the order of -30 MPa and $+15$ MPa respectively.

Finally (phase (III)), the four-point bending test simulation was carried out on the so assembled and post-tensioned reinforced composite system. At this stage, following phase (II), the adhesively bonded steel profile was again simply supported at the ends, in accordance with the experimental setup provided in Fig. 2. Lateral bracings able to prevent any out-of-plane deformation of the LG beam were also taken into account, in the form of nodal restraints.

Vertical displacements were assigned at the top edge of the glass layers, in order to reproduce the effect of the assigned bending loads during the experimental test, see Fig. 2. A displacement-controlled simulation was in fact carried out, by continuously monitoring the maximum mid-span deflection of the M0 post-tensioned system, as well as the maximum reaction forces at the beam supports, the distribution of principal stresses in all the FE model components and the possible propagation of damage in glass. The so defined vertical displacements were linearly increased up to a maximum value of ≈ 150 mm, in accordance with the ultimate vertical deflection experimentally observed for the full-scale test specimens (see Fig. 2(b)).

4. Validation of the M0 reference FE model

The M0 numerical model was first validated towards the load-deflection curves obtained from the past experimental test campaign, see Fig. 5 and Table 1.

In terms of overall performance, a rather interesting correlation was found between the FE predictions and the available experimental results, see Fig. 5.

A more detailed and critical analysis of the FE simulation results was first carried out by taking into account some key aspects of the mechanical performance of the examined experimental specimens, such as the initial uncracked stiffness K_{el} – i.e. the calculated slope

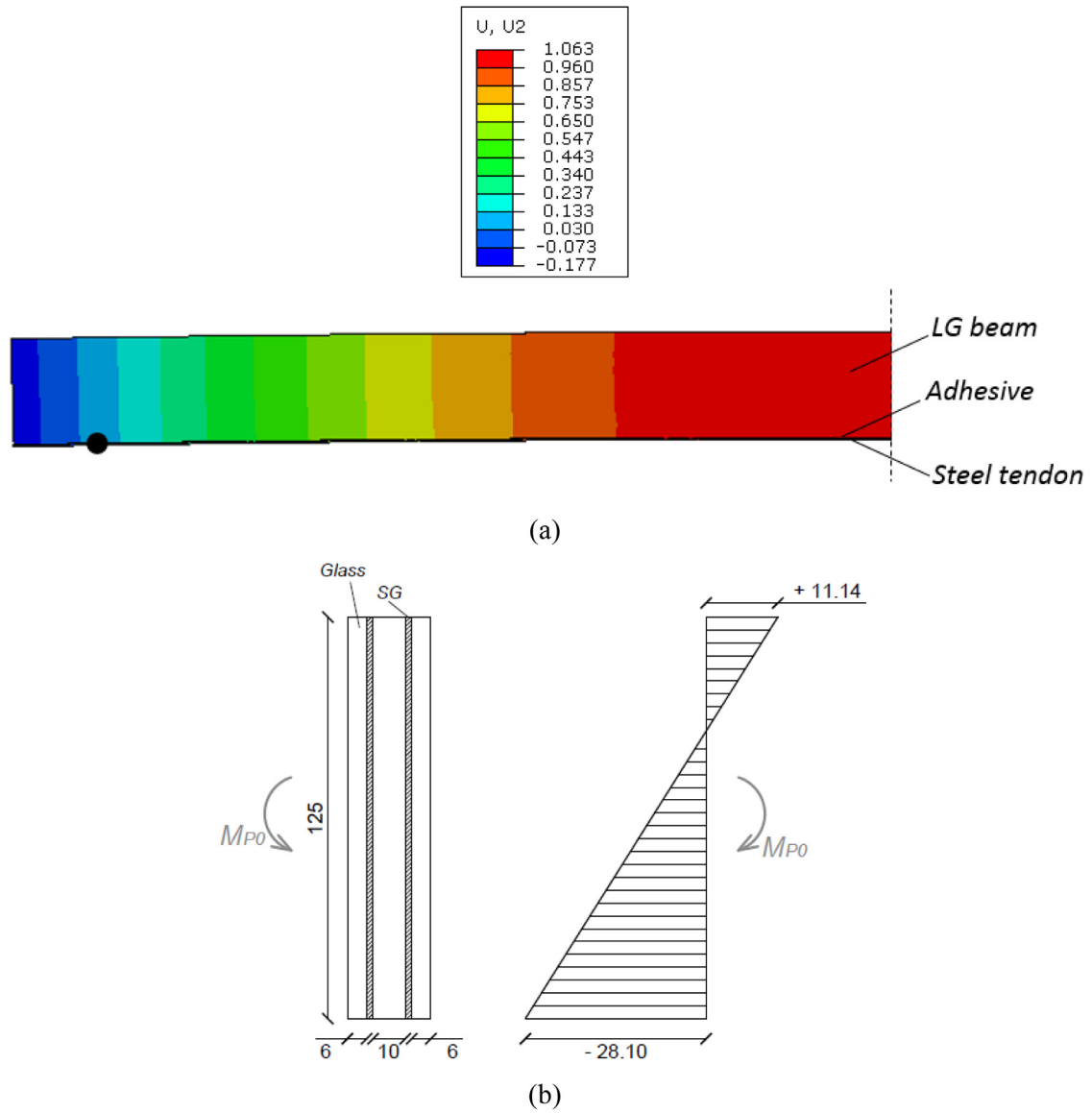


Fig. 4. Post-tensioning effects in the reference (M0) laminated glass beam only, as numerically predicted (ABAQUS [13]). (a) Beam deformed shape, front view of half beam only (scale factor = 5) and (b) corresponding distribution of initial stresses in glass (mid-span section). Values of deflections and stresses given in mm and MPa respectively.

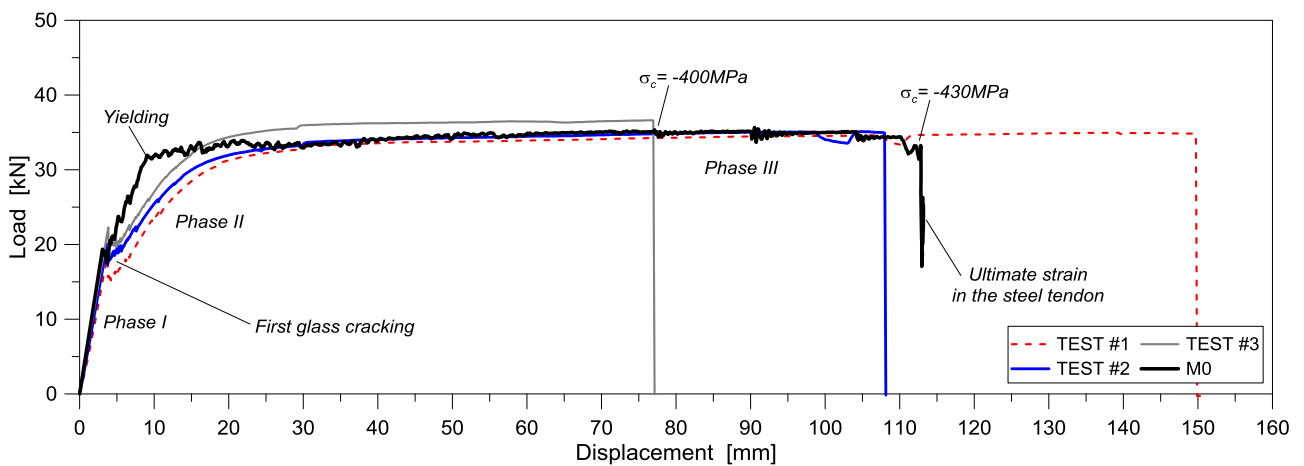


Fig. 5. Load-displacement curves for the reference post-tensioned glass beams, as obtained from the past experiments [1] and from the corresponding M0 numerical model [13].

Table 1
Bending performance of the M0 model [13], as compared with the average test results of the past experiments [1]. In square brackets, the range of variation for the experimental results is provided.

$\Delta = 100 \times (X_{FE} - X_{TEST})/X_{TEST}$	F_{1c} [kN]	u_{1c} [mm]	K_{el} [kN/mm]	F_{max} [kN]
TEST (average)	20.1	3.75	5.42	35.6
	[18.1–22.3]	[3.62–3.85]	[5.03–5.75]	[35.0–36.6]
M0 model	19.79	3.13	6.13	35.96
Δ [%]	1.54	16.5	13.0	1.01

of the available load-deflection data – of the so assembled and post-tensioned beams, the first cracking configuration (u_{1c} and F_{1c}), the maximum post-cracked load (F_{max}), as well as the post-cracked performance and the qualitative crack propagation and distribution in glass through the bending test simulation.

The FE curve proposed in Fig. 5, as also in accordance with the experimental findings given in [1], typically exhibits three specific phases, i.e. a fully elastic response of the composite section (phase I), an ultimate stage governed by the steel tendon only (phase III) and a transition phase (II) associated to progressive cracking of glass and yielding of the steel tendon. Compared to the experimental test results, where the average initial stiffness of the composite beams was found to be in the order of $K_{el} = 5.42$ kN/mm, the M0 numerical model provided an initial elastic slope $K_{el} = 6.13$ kN/mm, hence only partly overestimating ($\approx +13\%$) the experimental test results, see also Table 1.

Based on the experimental test data, the first cracks started to open at the bottom edge of glass panels at an average applied load $F_{1c} = 20.1$ kN, corresponding to a mean vertical deflection $u_{1c} = 3.75$ mm. The M0 numerical model properly captured the first cracking load, i.e. being this latter one equal to $F_{1c} = 19.79$ kN. Due to the partial overestimation of initial stiffness K_{el} , the corresponding deflection was found to be slightly lower than the reference experimental value, i.e. in the order of $u_{1c} = 3.13$ mm but in any case suggesting a close correlation between the experimental and numerical comparative results.

After glass cracking, both for the experimental specimens and the M0 model, the steel tendon provides a key contribution for the overall bending performance of the examined beam typology, since it provides additional post-cracked resistance and ductility. As far as the steel section almost represents – through the cracked stage – the only resisting component for the examined beams, the residual strength of such specimens is also strictly related to the cross-sectional dimension of the tendon itself. This aspect further justifies the close match between the FE results and the past experiments, since it can be noticed from Fig. 5 that the ultimate resistance was found to be equal to $F_{max} = 35.96$ kN and $F_{max} = 35.6$ kN (average value) for the FE model and the experimental tests respectively.

In the case of the first cracking stage only (i.e. phase II), the FE model tends to overestimate the corresponding test data (i.e. post-cracked stiffness). This effect, already emphasized in past numerical investigations carried out on steel-reinforced glass beams (i.e. [16], etc.), could be justified by some simplifications in the assumed smeared *brittle cracking* damage model for glass, as well as by possible local effects not properly captured by the basic assumptions (in terms of adhesive/SG constitutive laws and mechanical interaction between the 3D assembly components) of the actual FE models (i.e. delamination and viscous phenomena occurring in some regions of glass affected by major cracks, both at the glass-to-SG and glass-to-adhesive interfaces).

In this regard, the reference M0 model provided a crack propagation and distribution over the beam span typically associate to a large number of small cracks, as in the case of the reference experiments, with almost uniform propagation of cracks through the

beam thickness. Fig. 6(a) and (b) present the typical distribution of cracks in glass at collapse, as obtained from all the experimental specimens (with exemplificative picture provided for TEST #1 only) and the M0 model (with adhesive layer and steel tendon hidden from the view), including (Fig. 6(c)) the corresponding vectorial representation of compressive stresses in glass only.

As shown in Fig. 6(a), the test specimens typically exhibited at collapse a clear debonding of the steel tendon from the LG beam, in addition to the large number of cracks in glass. Based on this experimental observation, careful consideration was hence paid to further assess the validity of the FE modelling assumptions for the M0 model, i.e. by investigating the collapse configuration.

As far as the assumed *brittle cracking* model does not allow to impose a fixed limit for the compressive strength of glass and a corresponding damage material model, the minimum envelope of compressive stresses occurring in the whole glass layers was first monitored through the full simulation process, by taking into account the amount as well as the distribution of major peaks of stress. As shown from Figs. 5 and 6, the maximum compressive stresses were found to be in the order of -430 MPa, and typically located at the top edge of glass, close to the mid-span region. Additional peaks of compressive stresses, although limited in amplitude, were observed also in vicinity of glass cracks, see Fig. 6, as well as close to the beam end restraints. In any case, the monitored compressive stress values in glass were found to be typically lower than the corresponding nominal resistance of the material, namely in the order of -1000 MPa, as well as in agreement with other numerical research investigation on similar structural glass beams (see for example [16]).

Regarding Fig. 5, the numerical load-deflection curve clearly exhibited a drop at a mid-span displacement of ≈ 112 mm. The reason of this drop was found in the attainment of the ultimate strain in the steel tendon – i.e. close to a glass cross-section affected by major cracks, see point F in Fig. 6(b)) – which started to yield at a vertical beam deflection of ≈ 9 mm.

In terms of SG foils, limited stresses only were typically observed through the full bending simulation, i.e. with maximum local peaks of stress (typically attained in the same position of glass cracks, i.e. Fig. 6(b)) in the order of ≈ 50 MPa at the ultimate stage of the bending performance.

A further attempt of validation and assessment of the reference M0 model towards the experimental test results was finally carried out by taking into account the variation of stresses and strains in the adhesive layer, being this latter one of primary importance for the structural performance as a full composite system for the given resisting cross-section. As far as the implemented M0 model does not account for possible delamination at the level of the adhesive joint-to-glass or steel interfaces, the maximum shear stresses occurring on the top/bottom surfaces of the adhesive layer were in fact properly monitored. Fig. 7, in this context, presents the variation of the so calculated maximum stresses (envelope along the full beam span), as numerically estimated from the M0 model, together with the corresponding average value. Both the stress curves are proposed as a function of the beam mid-span deflection. As shown, limited stresses were generally found in the full adhesive joint, i.e.

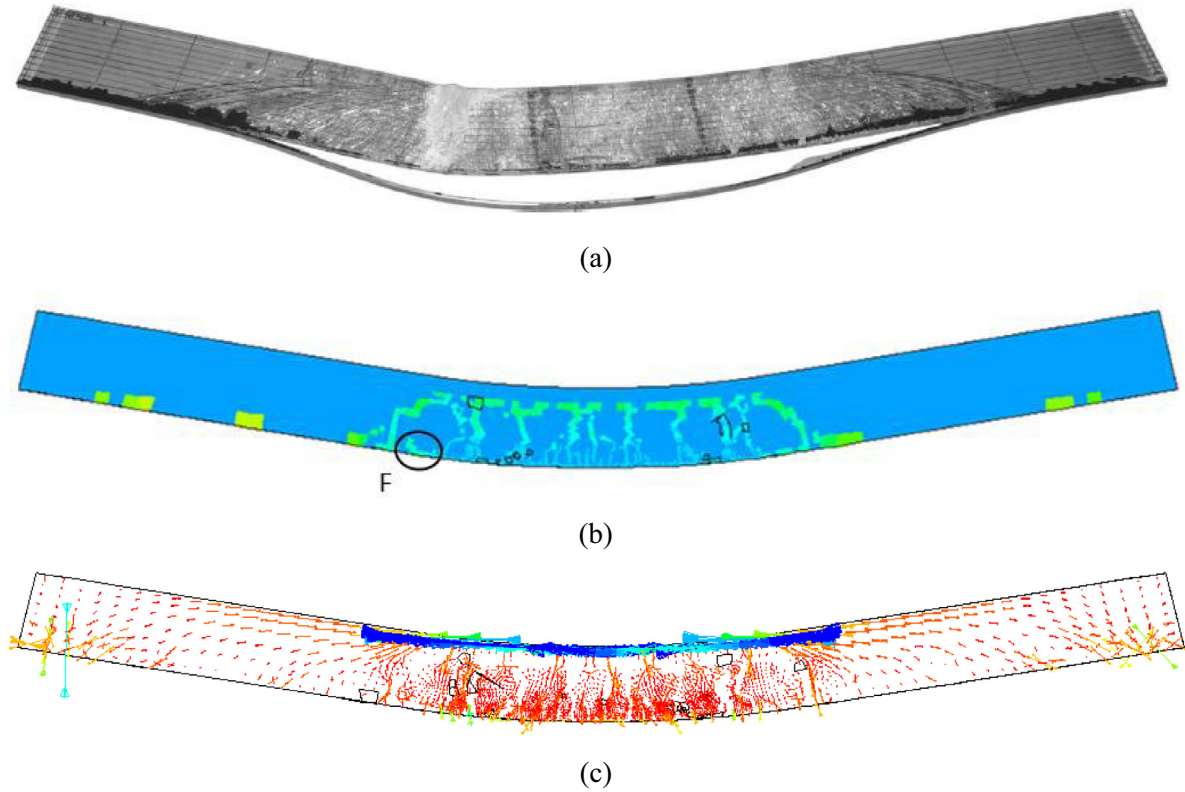


Fig. 6. Typical configuration of cracks in glass, as observed (a) experimentally [1] and (b) numerically from the M0 model (scale factor = 1), front view, with (c) corresponding distribution of compressive stresses in glass (vectorial representation).

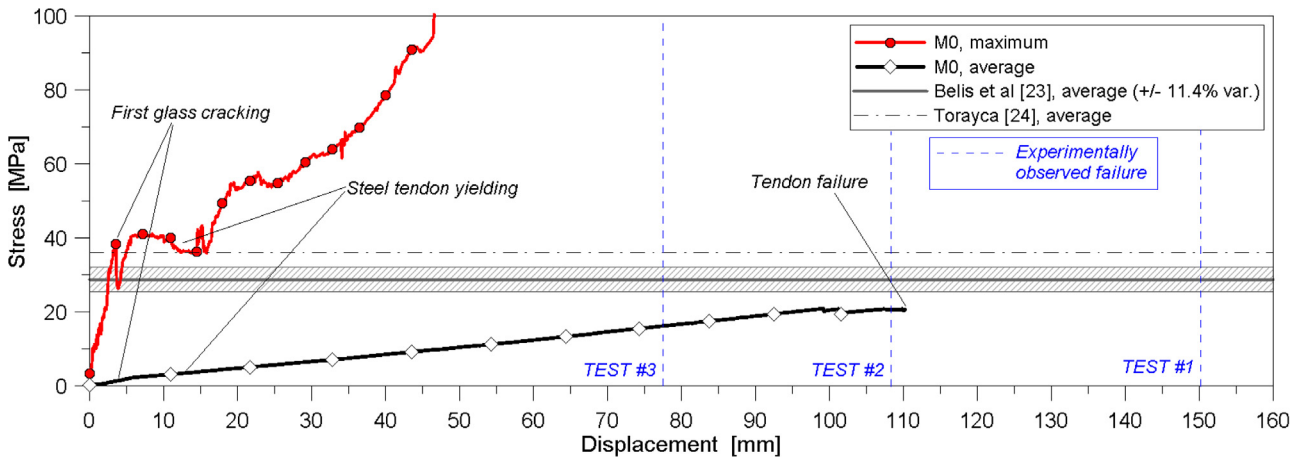


Fig. 7. Variation of average and maximum (point F of Fig. 6(b)) shear stresses at the top/bottom faces of the adhesive layer, as a function of the beam mid-span deflection, as numerically predicted by the M0 model.

in the order of ≈ 20 MPa at collapse. Markedly high peaks of stress were indeed observed in few locations only, i.e. were maximum plastic strains were attained in the steel tendon after yielding. In particular, the maximum envelope of stresses provided in Fig. 7 was found to be located in the same region of point F given in Fig. 6(b), i.e. where the steel tendon failed. After first glass cracking, an almost linear dependency to the beam mid-span deflection was found for the maximum envelope of stresses, increasing up to ≈ 500 MPa at the beam collapse.

Since the resistance of the adhesive connection strictly depends on the adhesive type as well as on the adherend properties, the so collected maximum and average stresses in the adhesive joint are

further compared in Fig. 7 with some reference shear strength values, as experimentally calculated in [23] for glass-to-aluminium 3M DP490 adhesive connections (mean experimental value, with evidence of its range of deviation), as well as provided by the adhesive manufacturer, in the case of adhesive connections to plastics [24]. As shown, after yielding of the steel tendon, the maximum stresses in the adhesive typically exceed the provided reference strength values, hence suggesting the possible initiation of debonding phenomena as experimentally observed. In this sense, this latter aspect should be properly assessed via additional experimental and numerical investigations on small scale specimens as well as full-scale assemblies.

5. Extended FE parametric study

An extended FE parametric investigation was then carried out, in order to achieve some additional suggestions on the structural performance of the examined beam typology, as a function of some key input parameters like the level of initial force in the tendon P_0 , the resisting section of the steel tendon (i.e. thickness), the type and thickness of the adhesive joint (i.e. shear stiffness of the bonding layer).

Despite the geometrical or mechanical variations in the FE models, the same general solving approach described in Section 3 was followed through the full parametric investigation. The major output of this extended numerical investigation is summarized in the following sections.

5.1. Adhesive joint size and type

Compared to the reference M0 model, the mechanical and geometrical properties of the adhesive joint interposed between the LG beam and the steel tendon were first modified, by fixing the geometrical and mechanical input data for the other beam components as well as the level of initial post-tensioning load P_0 .

Table 2 and Fig. 8 present the main features of the examined FE models, together with the corresponding comparative results.

As in the case of the M0 model, the MA-1 to MA-4 adhesive properties were described in the form of an ideal linear elastic constitutive law, see Section 3.2.2. A further adhesive type of large use in structural glass applications, i.e. a 3M 7271 Epoxy/Acrylic joint type, was also considered. In this latter case, a linear elastic law was again used, based on [22], with $E_{adh} = 1142$ MPa and $\nu_{adh} = 0.29$ the reference experimental values for the modulus of elasticity and Poisson ratio respectively. As in the case of 3M DP490 Epoxy, the latter adhesive type is typically characterized by a linear elastic response (see also [22] for the full experimental findings), hence suggesting the validity of the FE assumption for the purpose of the actual research investigation.

In terms of overall performance of the explored beams, the input parameters summarized in Table 2 manifested important effects, as expected, due to the key role of the adhesive joint features on the overall performance of glass assemblies and hybrid systems in general [25,26]. As far as the thickness and / or the shear stiffness of a given adhesive layer modifies, the level of bonding between the steel tendon and the laminated glass beam modifies, with clear effects on the post-tensioning phase as well as on the full bonding performance of the so assembled beams.

In accordance with [27], in fact, the shear effectiveness of the examined adhesive joints can be expressed via the non-dimensional parameter γ :

$$0 \leq \gamma = \frac{1}{1 + \frac{\pi^2 E_{steel} A_{steel}}{L^2 G_{adh} \tau_{adh}}} \leq 1, \quad (4)$$

where E_{steel} , A_{steel} and L are the modulus of elasticity, the resisting cross-section and the beam span respectively, G_{adh} is the adhesive shear modulus, $b_{adh} = 25$ mm the adhesive joint width (coinciding with the total thickness of the laminated glass section) and t_{adh} its thickness.

The so know “ γ -method” given by Eq. (4) – where $\gamma = 1$ for fully rigid and $\gamma = 0$ for flexible connections respectively – represents a standardized approach in current design practice (especially for timber-concrete composite structures, see for example the Annex B of Eurocode 5 [28]) and was originally proposed in [27] for composite beams with elastic shear mechanical connections. Given the shear stiffness and strength of a mechanical connection in a composite stiffness with partial interaction, the method is capable to estimate the corresponding effective bending stiffness. As basic assumptions of the approach, the composite beams object of analysis are simply supported, the individual parts span over the full length, the individual members of the composite beam are connected by a shear connection with uniform slip modulus, the spacing of mechanical connectors is constant or varies uniformly, according to the shear force and the applied external load gives a bending moment that is sinusoidal or parabolic.

In the current study, being the shear connection composed by a continuous adhesive joint with assigned geometrical features and elastic stiffness, based on Eq. (4) it can be seen that the increase of the bonding layer thickness t_{adh} typically results for a general composite beam in a weaker shear connection – i.e. with linearly dependent stiffness and theoretical effectiveness γ on t_{adh} – between the steel tendon and the upper beam. As a result, for a fixed level of initial force P_0 , a moderate reduction of the beneficial effects deriving from the post-tensioning phase would be expected to observe in the glass layers.

In this specific study, given the mechanical properties of the 3M DP490 epoxy layer for the M0 to MA-4 models of Table 2, the γ non-dimensional parameter was calculated in accordance with Eq. (4). As shown, the thickness increase resulted in a slight reduction of the expected shear stiffness efficiency for the adhesive connection, but with limited variations only.

Nevertheless, positive effects were observed when increasing the reference adhesive thickness t_{adh} . The maximum tensile and compressive stresses at the top and bottom edges of the mid-span glass section due to P_0 only (i.e. end of step II) were found to almost linearly increase when increasing t_{adh} , with maximum variations up to 11.62 MPa (top edge) and -29.03 MPa (bottom edge) respectively in the case of the MA-4 model (with 3 mm of adhesive), compared to the M0 beam (i.e. $\approx 4\%$ of initial stress increase due to the post-tensioning phase only). These findings are also in agreement with the analytical model presented in [1], due to the increased load eccentricity of P_0 from the beam neutral axis, as a consequence of the increased adhesive thickness. In terms of bending performance, see also Fig. 8 and Table 2, within the transition from the M0 model towards the MA-4 one, an almost

Table 2
Input parameters for the FE models, as obtained by changing the adhesive joint properties.

	FE Model #	Model properties			Bending test			
		Adhesive thickness [mm]	Adhesive type	γ (Eq. (4))	F_{1c} [kN]	u_{1c} [mm]	K_{el} [kN/mm]	F_{max} [kN]
Joint size	M0	0.1	3M DP490 Epoxy	0.9989	19.79	3.13	6.13	35.96
	MA-1	0.5		0.9945	18.14	2.94	6.13	37.17
	MA-2	1		0.9891	18.05	2.92	6.14	35.84
	MA-3	1.5		0.9838	18.01	2.92	6.15	36.57
	MA-4	3		0.9680	18.00	2.89	6.16	42.05
Joint type	M4-5	0.1	3M 7271 Epoxy/Acrylic	0.9995	19.60	3.25	6.14	34.66

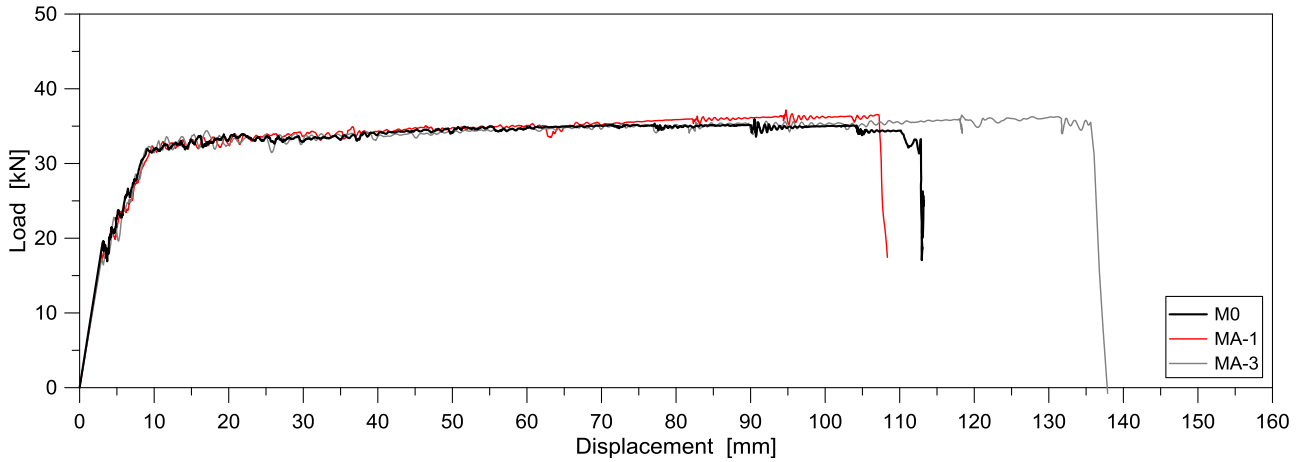


Fig. 8. Load-displacement curves for the M0 and MA-*i* models, by changing the adhesive joint properties.

linear increase of initial elastic stiffness K_{el} was also observed, up to $\approx 16\%$ due to the increased adhesive thickness and to the enhanced inertial properties (i.e. second moment of area I_y) of the composite resisting section. As a result, the inertial enhancement of the composite section was found – given the input geometrical and mechanical properties for the current study – to be the predominant aspect associated to the adhesive thickness variation, in terms of post-tensioning phase and the elastic phase of the bending test only.

While the post-tensioning beneficial effects are proportional to t_{adh} for the LG section subjected to a given initial force P_0 , however, as far as the bending deflection increases, the beam performances collected in Table 2 and Fig. 8 are primarily affected by the shear bonding capacity of the adhesive joint. Due to the reduced shear efficiency of the FE models with increasing adhesive thicknesses (Eq. (4)), as a result, the major benefits of the post-tensioning phase alone almost vanish at large bending deflections. Compared to the first cracking load F_{1c} of the M0 model, a linearly decreasing factor up to ≈ 1.1 times the M0 model value was observed for the MA-4 model with 3 mm of adhesive, hence resulting in an expected fracture load for that beam equal to 18.01 kN only at a mid-span deflection of 2.89 mm.

No marked effects were observed in terms of post-cracked performance for the models listed in Table 2, i.e. in the form of cracked stiffness variations and crack propagation / distribution in the glass beams. An almost constant ultimate residual strength F_{max} was also observed for all the examined models, due to the presence of a constant cross-sectional area for the steel tendon.

In the case of the MA-5 model with stiffer adhesive type, compared to the M0 model, close correlation was again found with the already commented behaviors.

5.2. Steel tendon section

At a second stage of the FE parametric investigation, the cross-sectional dimension of the steel tendon was considered as a key

parameter for additional numerical models, compared to the M0 model (see Table 3).

In order to quantify the effects of a different steel section only, the same level of initial strain $\epsilon_{M0} = f(P_0, A_{steel}, E_{steel}) = 0.002$ assigned to the reference M0 tendon was considered also for the MS-*i* models. As a result, the corresponding initial force value and the imposed equivalent elongation were properly calculated for each one of them. Given the $R\sigma_0$ stress ratio for the reference M0 model:

$$R\sigma_0 = k \cdot \frac{E_{steel}\epsilon_{M0}}{\sigma_y} = \frac{(t_{steel})_{MS-i}}{(t_{steel})_{M0}} \cdot \frac{E_{steel}\epsilon_{M0}}{\sigma_y}, \quad (5)$$

see Table 3, the imposed initial axial stress and strain were linearly increased with increasing the steel tendon thickness t_{steel} . A direct effect of this assumption was given by a high level of prestress for the MS-3 model, with assigned post-tensioning force leading the tendon close to yielding before the bending test simulation ($R\sigma_0 = 0.821$).

As shown in Table 3, the variation of the steel tendon thickness, based on Eq. (4), does not markedly affect the theoretical shear capacity of the adhesive connection. On the other hand, while a positive effect is expected in terms of overall structural performance for the MS-*i* models (both in the elastic and post-cracked stages), due to the increasing contribution of the steel tendon, the post-tensioning level was found to be the major influencing parameter for the bending performance of the beams.

In terms of pre-stressing and release phases only, a linear increase of initial tensile and compressive stresses at the top and bottom edges of glass was observed for the MS-*i* models, compared to Fig. 4, with maximum tensile/compressive stress values up to +38.5 MPa and –97 MPa for the MS-3 beam.

Regarding the in-plane bending performance of the same FE models, see Fig. 9, as far as same level of initial strain was imposed to the steel tendons, first yielding almost occurred at a comparable mid-span deflection for all the examined models (≈ 8.5 –9 mm).

Table 3

Input parameters for the FE models, by changing the steel tendon thickness, with $P_0 = 30$ kN.

FE Model #	Model properties				Bending test			
	Steel tendon thickness [mm]	Initial force level	$R\sigma_0$ (Eq. (5))	γ (Eq. (4))	F_{1c} [kN]	u_{1c} [mm]	K_{el} [kN/mm]	F_{max} [kN]
M0	3	P_0	0.410	0.9989	19.79	3.13	6.13	35.96
MS-1	4	1.78 P_0	0.547	0.9985	28.14	4.25	6.50	44.47
MS-2	5	2.78 P_0	0.684	0.9982	36.79	5.27	6.85	53.18
MS-3	6	4 P_0	0.821	0.9978	50.89	7.04	7.20	63.42

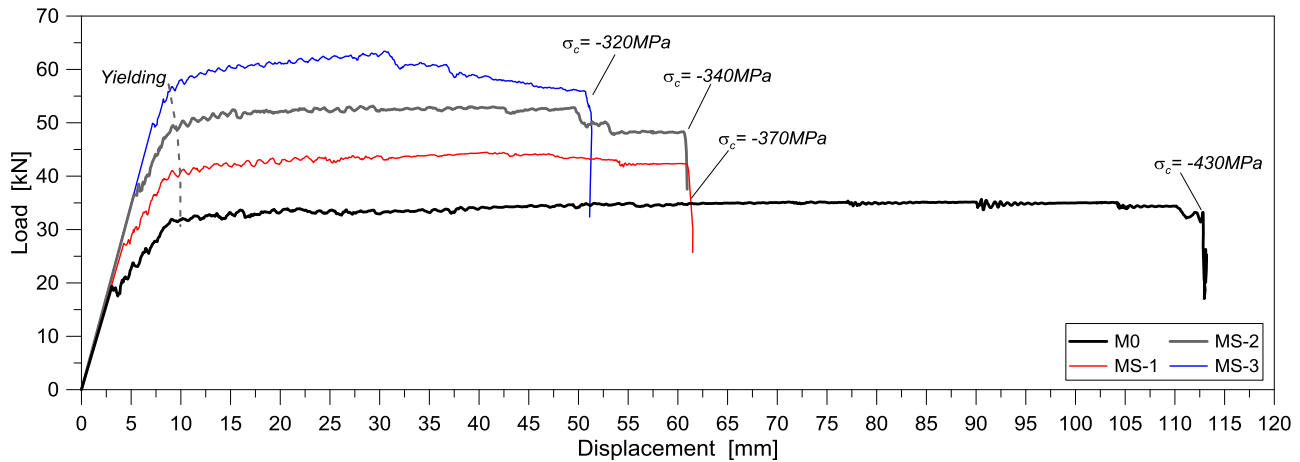


Fig. 9. Load-displacement curves for the M0 and MS-*i* numerical models, by changing the steel tendon section.

The positive effect of an increased steel tendon thickness is typically expected to be given by an increase of the maximum first cracking load F_{1c} and post-cracked resistance F_{max} for the same beams, see Table 3 and Fig. 9. The increase of steel tendon section for a fixed level of initial post-tensioning strain, however, coincides with a loss of redundancy for the examined beams, with ultimate strains in the tendons prematurely attained in the beams with higher steel sections. The observed effect is in close correlation with the performance of post-tensioned reinforced concrete members, where as far as the amount of steel and post-tensioning force exceeds a given ratio of the concrete section, a loss of ductility is typically observed [29]. The same effect is also in agreement with the past numerical investigations carried out in [9] on LG beams with mechanically anchored steel reinforcement tendons, where an optimal range of steel amount and post-tensioning force was preliminary detected. From Fig. 9, given the μ non-dimensional coefficient calculated as the ratio between the mid-span deflection at ultimate strain for the steel tendon and the mid-span deflection at yielding u_{1c} , a value comprised between 12.66 and 6.05 was in fact obtained for the M0 and MS-3 models respectively, hence linearly varying with the steel tendon thickness t_{steel} .

Compared to the crack pattern proposed in Fig. 6(b), finally, no marked variations were observed for the MS-*i* models, neither in the propagation or in the distribution of cracks along the beam span, as well as in terms of overall collapse mechanism. In terms of maximum stresses along the top and bottom faces of the adhesive joint, finally, slight effects were only found by changing the steel tendon thickness compared to Fig. 7, i.e. with average and maximum stress values at collapse in the order of 15 MPa and 550 MPa (in few localized sections only of the steel tendon) respectively for the MS-3 model with 6 mm thickness.

5.3. Initial post-tensioning level

A final attempt was carried out by taking into account several steel tendon thicknesses, in accordance with Section 5.2, and also various levels of imposed post-tensioning strain, i.e. in the order of 1/3 and 2/3 respectively the effects of the assigned P_0 value for the M0 reference model. The major input data and FE outcomes are summarized in Table 4 and Fig. 10.

In terms of overall performance for the explored set of beams, the collected FE results highlighted a major effects of the steel tendon section only in terms of elastic stiffness K_{el} and ultimate resistance F_{max} for the same beams. This find is in agreement with previous sections as well as with Eq. (4), since the expected theoretical effectiveness of the used adhesive connection is slightly affected only by the input parameters of Table 4 and generally suggests the presence of an almost fully rigid connection between the LG beams and the bottom steel tendons. Major variations, as also highlighted in Fig. 10, were observed when changing the initial pre-stressing level for a given cross-section with fixed geometrical properties. In this latter case, compared to Table 3, a primary effect was in fact derived from the reduced compressive state induced at the post-tensioning stage, with obvious consequences in terms of first cracking load for the examined beams.

In terms of ultimate collapse configuration, despite an almost regular and stable failure mechanism was generally observed through the full FE parametric investigation (i.e. see Fig. 6), no direct correlation was found between the assigned mechanical and geometrical input parameters and the corresponding ultimate deflection for the same FE models. In this latter case, localized failure in the steel tendons was in fact typically found to be associate to the propagation and distribution of few major cracks in glass at

Table 4
Input parameters for the FE models, by changing the steel tendon thickness and the initial pre-stressing level (with $P_0 = 30$ kN).

FE Model #	Model properties				Bending test			
	Steel tendon thickness [mm]	Initial force level	$R_{\sigma 0}$ (Eq. (5))	γ (Eq. (4))	F_{1c} [kN]	u_{1c} [mm]	K_{el} [kN/mm]	F_{max} [kN]
M0-P2	3	0.66 P_0	0.274	0.9989	16.37	2.61	6.13	34.4
MS-1-P2	4	1.19 P_0	0.365	0.9985	22.03	3.33	6.50	43.85
MS-2-P2	5	1.85 P_0	0.456	0.9982	29.36	4.22	6.85	53.24
MS-3-P2	6	2.67 P_0	0.547	0.9978	38.26	5.19	7.20	64.01
M0-P3	3	0.33 P_0	0.137	0.9989	14.39	2.34	6.13	35.4
MS-1-P3	4	0.59 P_0	0.182	0.9985	16.99	2.58	6.50	43.21
MS-2-P3	5	0.93 P_0	0.228	0.9982	21.72	3.15	6.85	54.02
MS-3-P3	6	0.33 P_0	0.274	0.9978	26.84	3.66	7.20	63.22

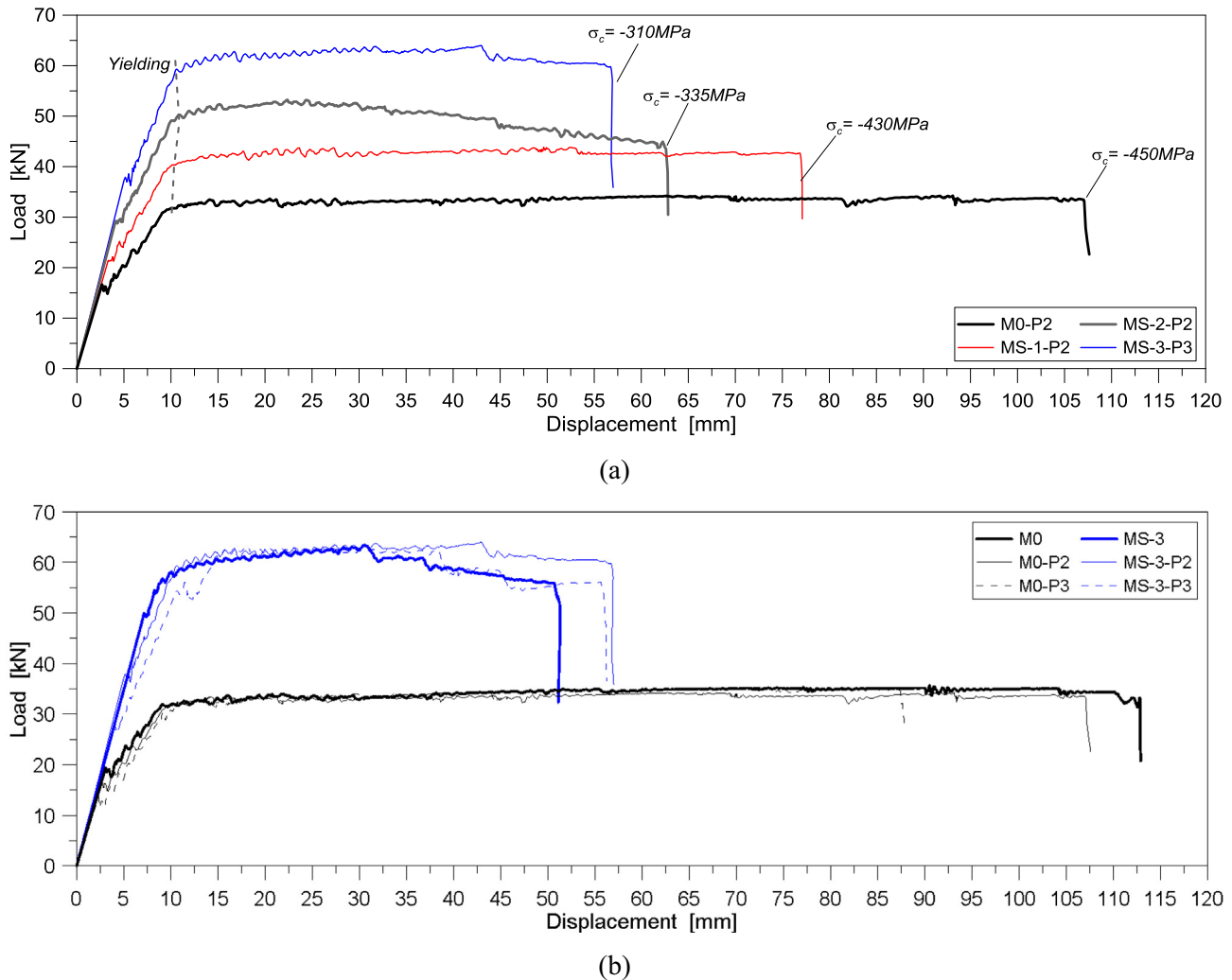


Fig. 10. Load-displacement curves for the M0 and MS-*i*-Pi numerical models. (a) MS-*i*-P2 models, by changing the steel tendon section; (b) FE models with 3 mm and 6 mm thickness for the steel tendon, by changing the initial pre-stressing level.

the ultimate stage only. For the same reason, maximum peaks of compressive stresses at the top of the glass layers were found – at the collapse configuration – to vary non-linearly with the steel tendon section or pre-stressing level variations. In any case, these maximum absolute values were always found to be in the order of 300–450 MPa for all the examined models.

6. Summary and conclusions

In this paper, the potential and feasibility of a structural glass beam concept consisting of post-tensioned laminated glass beams with adhesively bonded steel tendons has been explored by means of refined Finite-Element (FE) numerical models. Based on past experimental test results available for the same beam typology, a refined calibration and validation of a reference full 3D FE model was first proposed.

In doing so, careful consideration was paid for a multitude of geometrical and mechanical aspects of primary importance for a rational estimation of the overall structural performance of the examined beams, including advanced damage models (i.e. for the tensile cracking of glass) as well as a combination of mechanical interactions and imposed loads/displacements through the full FE numerical simulation. The final effect, as critically discussed in the paper, is a refined FE model type able to properly capture the

effects due to the assigned pre-stressing force, as well as the overall bending performance of the so assembled steel-reinforced laminated glass beam.

Based on the rather close correlation between the past experimental test results and the reference FE model, an extended parametric study was then also proposed, by varying the adhesive joint type and thickness, as well as the steel tendon section and pre-stressing level.

In general, the collected comparative FE results typically emphasized the high potential of the post-tensioning concept, since – as in agreement with traditional post-tensioned reinforced concrete members – the mechanical properties of glass can be fully exploited thanks to a combination of steel tendon and pre-stressing effects. As far as the steel section percentage exceed a given ratio of the glass resisting surface, however, the reinforcement benefits can vanish and manifest in a slightly ductile bending behavior, hence requiring further investigations for an appropriate optimization of the same design concept.

In any case, the overall FE investigation generally suggested a well promising structural performance for the examined beam typology.

It is expected, based on the current outcomes, that the presented FE modelling approach and parametric results could be further extended to fully assess the examined design concept,

including for example the effects of buckling phenomena, high-temperature performance, fatigue and cyclic effects.

References

- [1] Louter C, Cupać J, Lebet J-P. Exploratory experimental investigations on post-tensioned structural glass beams. *J Façade Desd Eng* 2014;2:3–18.
- [2] Bos F, Veer F, Hobbelman G, Louter C. Stainless steel reinforced and post-tensioned glass beams. In: Proceedings of ICEM12 – 12th international conference on experimental mechanics; 2012.
- [3] Jordão S, Pinho M, Martins JP, Santiago A, Neves LC. Behaviour of laminated glass beams reinforced with pre-stressed cables. *Steel Constr* 2014;7:204–7. <http://dx.doi.org/10.1002/stco.201410027>.
- [4] Engelmann M, Weller B. Post-tensioned glass beams for a 9m spannglass bridge. *Struct Eng Int* 2016;26:103–13. <http://dx.doi.org/10.2749/101686616X14555428759000>.
- [5] Cupać J, Louter C. Post-tensioned structural glass beams – comparative experimental study. In: *Proc Adv Build Skins*. p. 165–72 [USB drive].
- [6] Louter C, Cupać J, Débonnaire M. Structural glass beams prestressed by externally bonded tendons. p. 7–10 [USB drive].
- [7] Schober H, Gerber H, Schneider J. Ein Glashaus für die Therme in Badenweiler. *Stahlbau* 2014;73:886–92.
- [8] Bedon C, Louter C. Finite-element numerical simulation of the bending performance of post-tensioned structural glass beams with adhesively bonded CFRP tendons. *Am J Eng Appl Sci* 2016;9(3):680–91. <<http://thescipub.com/abstract/10.3844/ofsp.10781>>.
- [9] Bedon C, Louter C. Finite-element analysis of post-tensioned SG-laminated glass beams with mechanically anchored tendons. *Glass Struct Eng* 2016;1(1):39–59. <http://dx.doi.org/10.1007/s40940-016-0020-7>.
- [10] EN 572-2:2004. Glass in buildings – basic soda lime silicate glass products. Brussels, Belgium: CEN.
- [11] Martens K, Caspee R, Belis J. Development of composite glass beams: a review. *Eng Struct* 2015;101:1–15.
- [12] Martens K, Caspee R, Belis J. Development of reinforced and posttensioned glass beams: review of experimental research. *J Struct Eng* 2015. [http://dx.doi.org/10.1061/\(ASCE\)ST.1943-541X.0001453](http://dx.doi.org/10.1061/(ASCE)ST.1943-541X.0001453).
- [13] Simulia 2012. ABAQUS v. 6.12 computer software and online documentation, Providence, RI, USA: Dassault Systèmes.
- [14] Scotch M, Weld TM. EXPTM adhesive DP490 – product data sheet; 1996.
- [15] Louter C, Belis J, Veer F, Lebet JP. Structural response of SG-laminated reinforced glass beams; experimental investigations on the effects of glass type, reinforcement percentage and beam size. *Eng Struct* 2012;36:292–301.
- [16] Bedon C, Louter C. Exploratory numerical analysis of SG-laminated reinforced glass beam experiments. *Eng Struct* 2014;75:457–68.
- [17] Haldimann M, Luible A, Overend M. Structural use of glass. Zurich (CH): IABSE; 2008.
- [18] Martens K, Caspee R, Belis J. Numerical investigation of two-sided reinforced laminated glass beams in statically indeterminate systems. *Glass Struct Eng* 2016. <http://dx.doi.org/10.1007/s40940-016-0005-6>.
- [19] Ølgaard AB, Nielsen JH, Olesen JF. Design of mechanically reinforced glass beams: modelling and experiments. *Struct Eng Int* 2009;19(2):130–6.
- [20] Santarsiero M, Louter C, Nussbaumer A. The mechanical behaviour of SentryGlas® ionomer and TSSA silicon bulk materials at different temperatures and strain rates under uniaxial tensile stress state. *Glass Struct Eng* 2016. <http://dx.doi.org/10.1007/s40940-016-0018-1> [published online].
- [21] EN 1993-1-4. Eurocode 3–design of steel structures – Part 1–4: general rules – Supplementary rules for stainless steels; 2006.
- [22] Nhamoinesu S, Overend M. The mechanical performance of adhesives for a steel-glass composite façade system. In: Proceedings of challenging glass 3 – conference on architectural and structural applications of glass, TU Delft; June 2012.
- [23] Belis J, Van Hulle A, Out B, Bos F, Callewaert D, Poulis H. Broad screening of adhesives for glass-metal bonds. *Proc Glass Perform Days 2011*:286–7.
- [24] Torayca. T700 technical data sheet No. CFA-005, <<http://www.toraycfa.com>>; 2008.
- [25] Machalická K, Eliášová M. Adhesive joints in glass structures: effects of various materials in the connection, thickness of the adhesive layer, and ageing. *Int J Adhes Adhes*. <http://dx.doi.org/10.1016/j.ijadhadh.2016.09.007>.
- [26] Firmo F, Jordão S, Costa-Neves L, Bedon C. The effect of adhesive joints on the performance of hybrid steel-glass beams – an analytical and experimental study. In: Proceedings of challenging glass 5 – conference on architectural and structural applications of glass, Ghent, Belgium. USB drive; 2016.
- [27] Möhler K. Über das Verhalten von Biegeträgern und Druckstäben mit zusammengesetzten Querschnitten und nachgiebigen Verbindungsmitteln. TH Karlsruhe; 1956.
- [28] Eurocode 5 – design of timber structures – Part 1–1: general rules and rules for buildings. CEN 2004, Brussels, Belgium.
- [29] Dirk Bondy K, Allred B. Post-tensioned concrete: principles and practice. ISBN: 978-1-4834-0372-4.